RESEARCH METHODS PAPERS

QUANTIFICATION OF BIOTURBATION IN HEMIPELAGIC SEDIMENTS VIA THIN-SECTION IMAGE ANALYSIS

PIERRE FRANCUS*
Département de Géologie et Géographie, Université catholique de Louvain, Place L. Pasteur, 3, B-1348 Louvain-la-Neuve, Belgium
e-mail: francus@geo.umass.edu

ABSTRACT: **Traditional ichnofabric-descriptive (semiquantitative) schemes rely upon subjective estimates of the degree to which original sedimentary fabrics have been disrupted. This paper presents an objective method of quantifying bioturbation in hemipelagic sediments based on a thin-section image-analysis technique. In order to perform these analyses, optical or backscattered electron micrographs are processed in order to obtain black and white images. In these images black pixels are silt-size, larger grains and the clay-size sedimentary matrix are white pixels. Once the initial processing has been accomplished, an index, *H*, is defined to quantify the horizontal orientation of the larger grain size fraction of the sediment. *H* is low for bioturbated fabric and high for laminated sediments. In hemipelagic suspension deposits, *H* can be used to quantify bioturbation, assuming that no other sedimentary processes have disrupted the original depositional fabric. The quantitative bioturbation scheme described here is consistent with existing semiquantitative bioturbation schemes; in addition, it is objective and provides higher-resolution descriptions of biological processes that disrupted the sediment after deposition. Applying this quantitative scheme should refine future paleoecological reconstruction derived from lacustrine and marine successions.**

INTRODUCTION, AIM, AND RATIONALE

The amount, type, and distribution of bioturbation provide information about depositional conditions. Because these observations are very useful tools that aid the reconstruction of conditions at and shortly after deposition (e.g., Kennett and Ingram 1995; Savrda 1995), numerous qualitative and semiquantitative classifications of ichnofabric have been proposed (e.g., Reineck and Singh 1975; Savrda et al. 1984; Droser and Bottjer 1986; Miller and Smail 1997). These schemes have been widely used in paleoceanographic (e.g., Savrda 1995) and paleoclimatic (e.g., Behl and Kennett 1996) studies and in research on relative sea-level change (e.g., Taylor and Gawthorpe 1993). Unfortunately, they depend mainly upon visual estimates of sedimentary fabric, and this subjectivity inevitably introduces error into paleogeographic reconstruction. In order to minimize this source of error, this paper presents a quantification method, which is independent of subjective analyses, to define the degree of bioturbation. The method described here builds upon recent developments in thin-section image analysis (Francus 1998; Francus and Karabanov 2000) that quickly and objectively quantify how much the coarse sediment fraction deviates from the horizontal. In fine-grained hemipelagic sediments this deviation is assumed to measure the effects of bioturbation.

In order to generate a quantitative descriptive scheme of bioturbation, it is necessary to first describe the fabric of undisturbed hemipelagic sediments. With this in place the effects of bioturbation and other mechanisms of sediment disruption of the primary fabric can be assessed. Then, the validity of the *H* index and robustness of the image-analysis technique can be compared with measures obtained using existing semiquantification schemes. Finally, *H* index analysis is applied to recent hemipelagic sediments from Lake Baikal, Siberia, Russia (Francus and Karabanov 2000) and Lake Vico, Latium, Italy (Leroy et al. 1996) to test the robustness of the technique and provide working examples of the method.

BACKGROUND TO HEMIPELAGIC SEDIMENTATION

Hemipelagic sediments are believed to accumulate from fine particles suspended in the water column, which settle to the sediment–water interface (e.g., Grimm et al. 1996). In the sediment this process is thought to cause platy clay and coarser-grained particles that have not flocculated to be oriented subparallel to the sediment–water interface, forming an oriented, primary plasmic fabric (e.g., Kuehl et al. 1988). In clay-rich sediments deposited by flocculation, however, the depositional fabric is commonly more random and less well oriented (e.g., O'Brien and Pietraszek-Mattner 1998). Surprisingly, to our best knowledge, no laboratory experiments have been done to reproduce the primary settling fabric of hemipelagic sediments to corroborate this assessment. Extensive microscopic observation and review of published micrographs of hemipelagic sediments (e.g., Krinsley et al. 1998), however, reveals that elongated particles are commonly oriented mostly horizontally. Where elongated particles are not horizontally oriented, they are usually contained within aggregates or pellets that sedimented either directly from the epilimnion or from redeposition (Chang and Grimm 1999). These aggregates and pellets are easy to identify by thin-sectioning the sediment and then using either conventional optical or backscattered electron (BSE) methods to image the sediment fabric (e.g., Brodie and Kemp 1995).

The laminae that are characteristic of hemipelagic sediments are produced by variations in sediment input. In hemipelagic settings (in both marine and lacustrine settings) sediment is rarely supplied to the sediment–water interface as a slow continuous rain of debris. Instead, sediment-trap records unequivocally demonstrate that it is supplied episodically and/or seasonally and that these variations are linked to either variations in primary production or sediment flux (Grimm et al. 1996). In some settings the individual laminae are subtly graded. Where grading is present it is usually attributed to particle sorting in the water column (e.g., Stow and Bowen 1980; Lamoureux 1999). Subtly graded bedding, however, is not common, because clay minerals have settling velocities much lower than that of fine-grained quartz fraction (e.g. Doyle et al. 1983).

In hemipelagic sediments, bioturbation is the dominant source of syndepositional and postdepositional disturbance. It disrupts the primary fabric, causing it to exhibit a range of textures from ''slightly disturbed laminae'' to ''totally homogenized bedding of massive appearance'' (Droser and Bottjer 1986). Segall and Kuehl (1994) have produced a multi-scale description of some bioturbated sediment and shown that ''bioturbated sediments do not display grain orientation . . .''. On the basis of ^{234}Th mixing coefficients, Kuehl et al. (1988) reported that bioturbation-induced disruption of plasmic fabric suppresses the original preferred orientation. Finally, microscopic observations of bioturbated sediments (e.g., Brodie and Kemp 1995, fig. 8) reveal that the particles within them exhibit a random orientation. These observations suggest that *it should be possible to quantify bioturbation by estimating the disruption of the original horizontal fabric, assuming that other mechanisms that disrupt primary fabric can be de-*

* Present address: Department of Geosciences, University of Massachusetts, Amherst, MA, 01003, U.S.A.

JOURNAL OF SEDIMENTARY RESEARCH, VOL. 71, NO. 3, MAY, 2001, P. 501–507
 1073-130X/01/071-501/$03.00

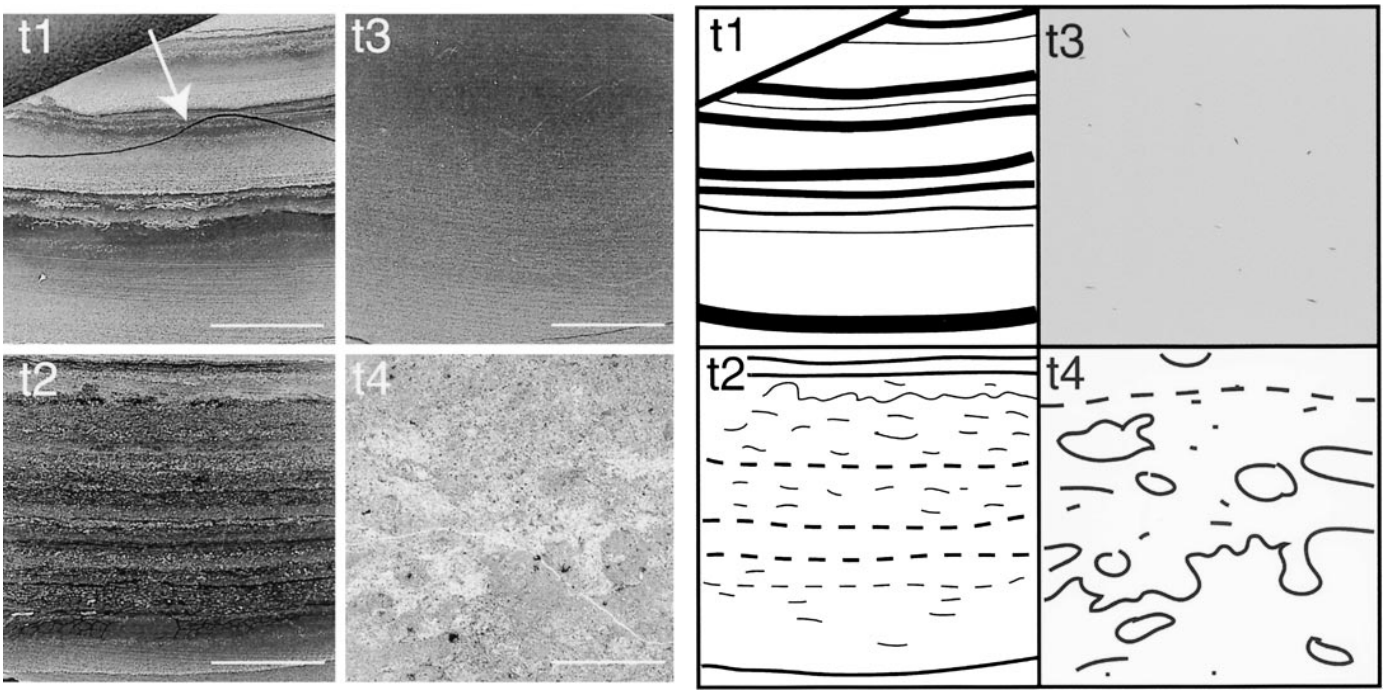

FIG. 1.—Ichnofabric categories. Left panel: high-resolution flatbed scanner view of impregnated sediment chip and thin section; scale bars, 1 cm. White arrow points to sharp crack due to the freeze-drying process. The crack does not affect the sediment fabric. Right panel: sketch of the fabric.

tected prior to measurements. Nonbiogenic disturbances can be easily disregarded by microscopic observation and careful sampling. The mechanisms that cause these disruptions include: (1) penecontemporaneous deformation that variously produces ball-and-pillow structures, flame structures (Reineck and Singh 1975; Beck et al. 1996), and intrastratal microfractured zones (Grimm and Orange 1997); (2) density currents, which may re-entrain the individual particles (Hohman et al. 1997) or form intraclasts (Chang and Grimm 1999); (3) compaction and distortion due to drilling and other drilling artifacts (N.B: compaction alone does not produce complete reorientation; Bennett et al. 1981); (4) gas bubbles in sediment cores due to the difference between gas pressure within the sediment and the atmospheric pressure; these are visible macroscopically; (5) growth of authigenic mineral assemblages (e.g., pyrite, vivianite, chert etc.) (Brauer and Negendank 1993; Wilkin et al. 1996), and (6) artifacts introduced during the thin-section preparation process, which are most easily avoided by careful preparation of the thin section, using low-viscosity epoxy resin (Lamoureux 1994; Pike and Kemp 1996).

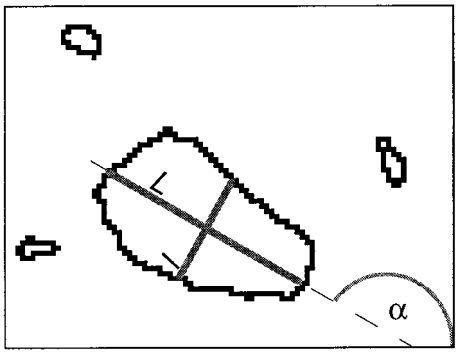

FIG. 2.—Detail of a binary image. Measurements on each object *i*: major (*L*) and minor (*l*) axes and angle α between horizontal and major axis *L*.

METHODS

Sampling

To minimize fabric disruption, thin sections were prepared from samples collected from soft-sediment cores obtained from Lake Baikal and Lake Vico, using a slightly modified freeze-drying technique described in von Merkt (1971) and Kuehl et al. (1988). This technique does not impart any orientation to the sediment fabric (Kuehl et al. 1988), although cracks may develop (Pike and Kemp 1996). Cracking, however, does not significantly affect the primary depositional fabrics, and, where present, the cracks can easily be recognized (Fig. 1).

Data Acquisition

To document the sediment microfabric, cover-slipped thin sections were analyzed with conventional petrographic methods, using both plane-polarized light and cross-polarized light. Thin sections were then uncovered and carbon-coated for electron microscope examination, using a scanning electron microscope equipped with a BSE detector. The microscope was operated at 20 kV and a working distance of 19 mm. Images of 512 $\times$ 512 pixels were digitized using the video output of the microscope. The epoxy resin used for impregnation of thin sections has a light atomic weight, and therefore a lower backscattered electron coefficient. The interacting volume between the beam and the specimen is only 1–2 μm deep (Krinsley et al. 1998), limiting the occur-

TABLE 1.—H *index values measured from six different micrographs of the same layer bed.*

Sample #	Micrograph 1	Micrograph 2	Micrograph 3	Micrograph 4	Micrograph 5	Micrograph 6
1	4.56	3.99	4.63	7.22	4.54	4.56
2	2.90	2.21	2.17	2.80	2.02	2.75
3	0.01	0.05	−0.02	0.03	0.01	−0.08

All samples from Lake Baikal. Sample #1: BDP93, 93/1, 5611 cm depth is classified as (t1), sample #2 STA 316, 461.6 cm depth is classified as (t2) and sample #3, STA 321, 72.3 cm depth is classified as (t4).

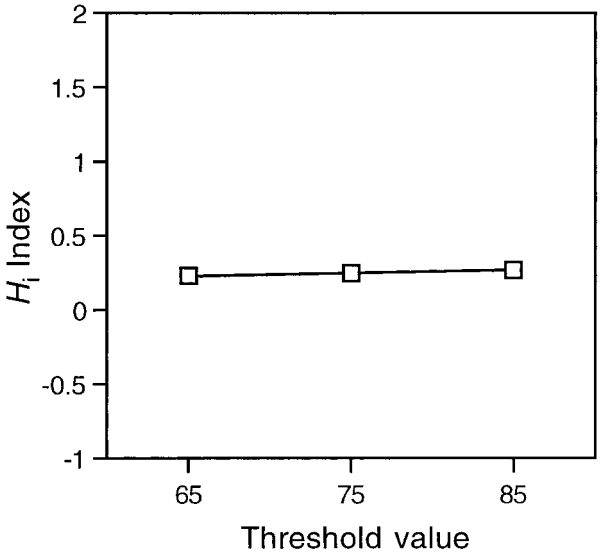

FIG. 3.—*H* index value variations using three different threshold levels on a test micrograph.

rence of object superposition. Digitized pictures were processed on a Power Macintosh computer, using the public domain NIH Image program (developed at the U.S. National Institutes of Health and available on the Internet at http://rsb.info.nih.gov/nih-image/). An image-analysis processing layout is applied to the 256 gray-scale BSE images: filtering to reduce noise (median filter/contrast/hybrid median filter), thresholding, and binary image edition (fill interior blanks/suppress less than 20 pixel objects/watershed segmentation) (Francus 1998; Russ 1999; http://www.geo.umass.edu/climate/francus/). Processing produces black-and-white images, where white pixels represent the clay-rich sedimentary matrix and black pixels represent objects (*i*) to be measured (e.g. clastic grains, organic debris, diatoms) (Francus 1998). On each object, *i*, the following are measured (Fig. 2): (1) the area (*A*), calculated by counting the number of contained pixels; (2) lengths of the major (*L*) and the minor (*l*) axes; and (3) angle (α) between the horizontal and the major axis *L*, measured counter-clockwise. Data are exported to a spreadsheet for further processing.

Index Definition

The size of the grains is estimated by the equivalent disk diameter, D_0 [as 1]:

$$D_0(\mu m) = 2\sqrt{\frac{A(\mu m^2)}{\pi}} \qquad [1]$$

where *A* is the area of the object (Francus 1998).

D_0 is not the real grain size, because the grain sphericity is an idealization and random thin-section cutting of spheres underestimates the diameter. Photograph magnification directly influences the size of objects that are perceptible (Bouabid et al. 1992; Russ 1999). Yet, if photographs are taken in similar conditions, D_0 measurements can be used to quantify variations in sediment apparent grain size (Francus 1998).

H_i is defined to quantify the horizontal disposition of each object *i* of sedimentary microfabrics on the digitized BSE picture. H_i is defined as [2]:

$$H_i = \left(\frac{L}{l} - 1\right)((2\cos(2\alpha))|\cos(2\alpha)|)\left(\frac{D_0 - MD_0}{sD_0}\right) \qquad [2]$$

where *L*, *l* and α are defined above; D_0 is the equivalent disk diameter, as

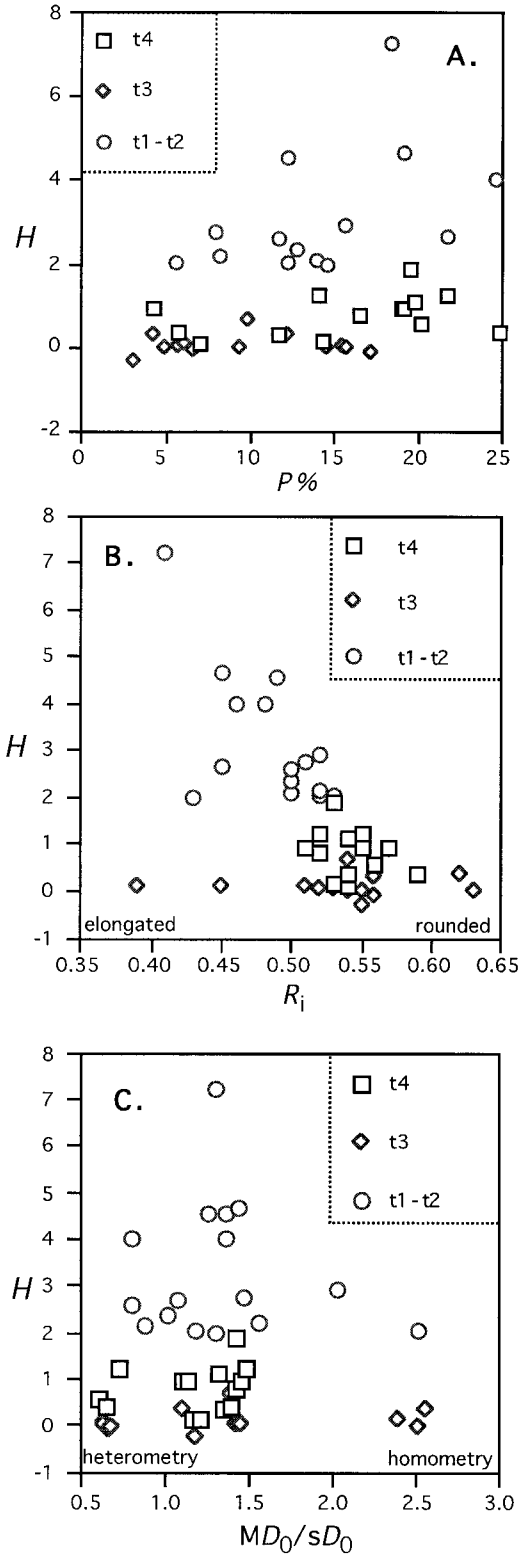

FIG. 4.—**A)** *H* vs. *P*% (*P*% = # black pixels/# pixels) for the 45 hemipelagic samples. *H* does not correlate with particle content. **B)** *H* vs. R_i ($R_i = 4A/\pi L^2$). R_i is strong for rounded objects and weak for elongated ones. *H* is independent of the shape of the objects. **C)** *H* vs. MD_0/sD_0 of the equivalent disk diameter (Francus 1998). Weak MD_0/sD_0 values are heterometric grain-size populations, whereas strong MD_0/sD_0 values are homometric grain-size populations. Bioturbation equally affects homometric and heterometric sediments.

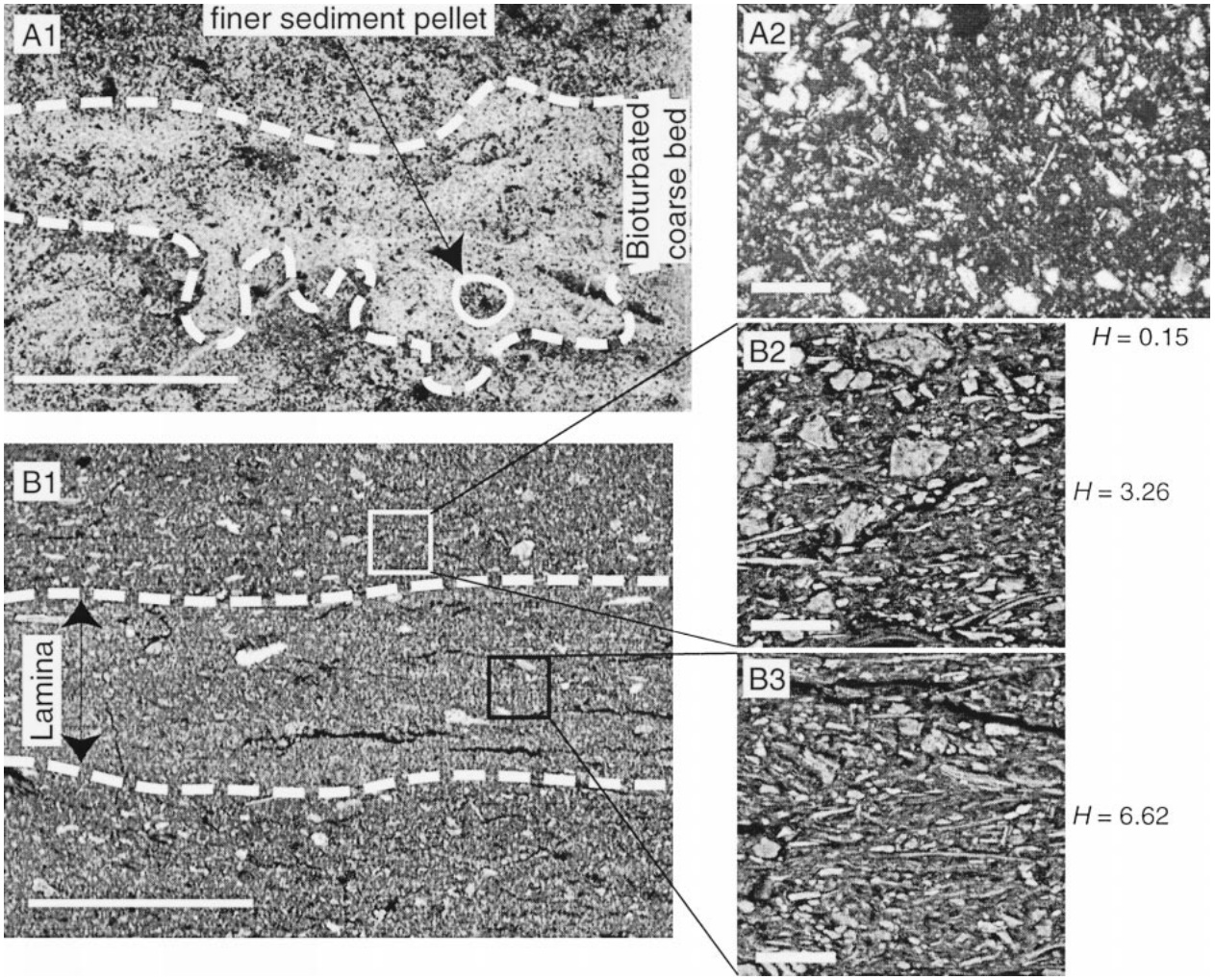

FIG. 5.—**A1)** Macroscopic view of a thin section: bioturbated coarse-silt bed. Lake Baikal, northern basin; scale bar, 5 mm. **A2)** Detail of the previous coarse bed, microscopic view (crossed-polarized light); scale bar, 100 μm. The silt grains are not horizontally deposited. H is weak: 0.15. **B1)** BSE image of a lamination at Buguldeika uplift: general view; scale bar, 500 μm. **B2)** Detail of the previous BSE image (white square) outside the lamina; scale bar, 50 μm. $H = 3.22$. **B3)** Detail of the previous BSE image (black square) inside the lamina; scale bar, 50 μm. $H = 6.62$. In comparison with B2, objects are more elongated and more horizontal; H is stronger. Gray-level intensity is different in micrograph A2 from those in B2 and B3, because the first is an optical-microscope view and the latter are BSE images. Francus (1998) shows that the image measurements can be compared.

in [Eq. 1]; MD_0 and sD_0 are the median and the standard deviation of D_0 for all the objects in one picture.

Three major parts can be detailed in the equation for H_i (Eq. 2). The first term in brackets produces high H_i values for elongated objects, whereas spheres produce an H_i value of 0. The second term in brackets is devoted to the angular information: high positive values (2) are assigned to horizontal objects, negative values (-2) are assigned to vertical ones, and zero (0) is assigned to objects at 45° or 135°. Multiplication by $|\cos(2\alpha)|$ necessary to reduce H_i for poorly horizontal objects that have α near but less than 45° or near but greater than 135°. The last part of the equation gives to H_i a value proportional to the object sizes. D_0 is normalized to allow comparison between microfabrics with different grain sizes. In brief, large elongated horizontal objects result in high H_i values, whereas small spherical ones result in low H_i values.

Index H quantifies the horizontality of the fabric. H is equal to the mean H_i, considering only objects that have a D_0 greater than MD_0. This selection is necessary for two main reasons: (1) the H index is calculated using the most significant elements of the sedimentary fabric: large grains are the ''skeleton'' of the fabric, and in classical orientation studies (Cheel 1991) only elongated and large grains are measured for the construction of rose diagrams. (2) The smallest grains are numerous in typical images. They have H_i values closer to zero, smoothing the final H value of the fabric and, therefore, preventing a clear discrimination of the sedimentary fabric using H.

Robustness of Image Analysis

To assess the method, it is necessary to check that sampling or image processing introduces no bias. First, because of the small size of the cross section, typically 850 × 550 μm, the selected field area is possibly not representative of the entire fabric. Measurements obtained repeatedly, using several micrographs to cover different areas of the identical fabric within some distinctive layers (Table 1), show similar H indices. This result shows the consistency and reproducibility of the method for the kind of sample studied here. This result is not surprising, because the number of particles measured on a single micrograph is commonly in the range 400–500. This is enough to have a representative sample of the particle population (Kennedy and Mazzullo 1991). Moreover, cross sections are large compared to

TABLE 2.—*Sedimentary characteristics of the ichnofabric categories used in this study. Types described here refer to Figure 1.*

Fabric Type	Description
Type 1	Well laminated fabric; no sign of biogenic activity; corresponds to type 1 of Droser and Bottjer (1986)
Type 2	Laminated fabric; minor disturbance of laminae; diffuse limit of laminae, minor sediment disruption; microbioturbation traces as described by Brodie and Kemp (1994)
Type 3	Homogeneous fabric; no primary fabric visible macroscopically; include sediment with plasmic fabric (Kuehl 1988)
Type 4	Bioturbated fabric; bed completely mixed; clay aggregates, nested structures, burrow traces; corresponds to types 3 to 5 of Savrda et al. (1984)

the size of the beds being measured in this study, between 400 μm and 1 cm in thickness.

Second, the image-analysis technique implies the choice of a threshold. This important step involves the selection of particles on the basis of their gray-level values (Francus 1998). This step could be highly subjective if images were not processed and filtered before thresholding (Russ 1999). Therefore, prior to thresholding every image is processed in the same way; this removes biases, which would otherwise be introduced by variations in contrast, background gray level, and irregular illumination (Russ 1999). Because typical images are bimodal, it is easy to fix the threshold level at the lowest point between the two modes. In any case, determinations of threshold level have been tested. In Figure 3, we varied the threshold value by 16% of the total gray-level range in a test micrograph. The resulting changes in the *H* index value are not significant.

Third, it was necessary to check that no bias was introduced by image analysis, sampling, or *H* index computation. This is not the case, because a large range of *H* index values are reported in sediments that are both rich and poor in silt-size grains (Fig. 4A), that are either rich or poor in elongated elements (Fig. 4B), and that are either homometric or heterometric sediments (Fig. 4C).

Classical Ichnofabric vs. H Index

To compare results obtained using image analysis with semiquantitative methods, each sample was classified according to the published schemes of Savrda et al. (1984) and Droser and Bottjer (1986), but adapted for our samples and for microscopic thin-section observations (Fig. 1, Table 2). Even though this classification scheme was designed for microscopic-scale observations, it is possible to link it to conventional ichnofabric analyses, because the samples were classified according to both mesoscale and microscale observation. Results from these comparisons suggest that samples with a high bioturbation index had low *H* values and laminated samples had a high *H* index (Fig. 5).

To equate the *H* index scale with conventional descriptive terms, measurements were performed on 45 samples from different hemipelagic environments from Lake Baikal (Fig. 6). These measurements display a consistent continuum of *H* values, ranging from intense bioturbation (t4 samples) to no bioturbation (t1 samples). High *H* values, between 2.0 and 7.5, correspond to nonbioturbated or weakly bioturbated types t1 to t2. Homogeneous (t3) fabrics range between 0.1 and 2.6, with overlapping with other categories. Samples with highest *H* values display minimum light transmission in thin sections when bedding is parallel to the polarizer, and maximum light transmission when bedding is oriented at 45° to the polarizer. They correspond to the plasmic fabric described by Kuehl et al (1988). At the other extreme of the bioturbation scale, strongly bioturbated sediments (t4) correspond to the lowest *H* values, between 0.34 and −0.29. In order to determine if measurements taken from remote locations are comparable, 58 samples from Lake Vico were also measured. Figure 7 displays together *H* index values of samples from both lakes. The pattern is similar to the one obtained in Figure 6.

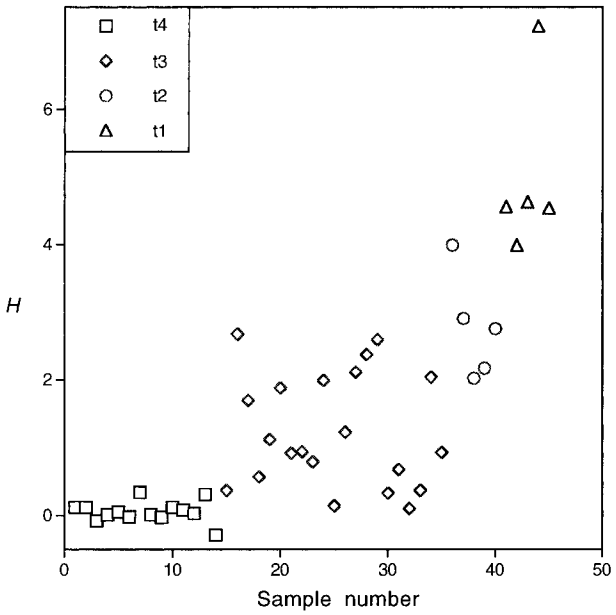

FIG. 6.—*H* for 45 samples from hemipelagic environments sorted according the semiquantification scheme described in Figure 1: t1 are laminated fabrics without bioturbation traces; t4 are strongly bioturbated fabrics.

DISCUSSION

Results displayed in Figures 5, 6, and 7 establish the validity of the methodology. Not surprisingly, laminated (t1) fabric samples have the highest *H* values. Overlapping between conventional and *H* values, seems to be a limitation, but further interpretation reveals, to the contrary, the proficiency of the methodology: the *H* values of microbioturbation (t2) fabric can be as low as the *H* values of the macrobioturbated (t4) fabric. On the other hand, some other microbioturbation (t2) fabric samples show *H* values as strong as (t1) laminated fabric. This is because the intensity of the microbioturbation is not uniform. For instance, lateral fading of laminae

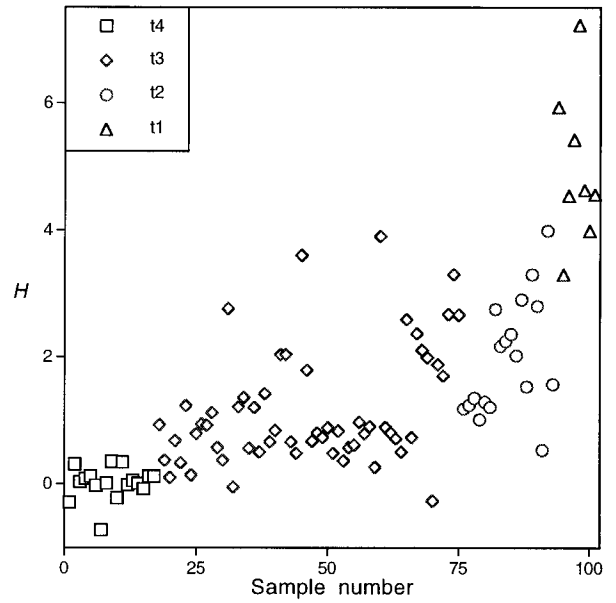

FIG. 7.—*H* for 103 samples from Lake Baikal, Siberia, Russia, and Lake Vico, Latium, Italy.

could be interpreted as the result of the heterogeneity of the microbioturbation (Brodie and Kemp 1994). The (t3) samples with the highest *H* values ($H = 3.93$) display the plasmic fabric. They are interpreted as being a primary fabric (Kuehl et al. 1988), little affected by bioturbation. Type 3 samples having the lowest *H* values (for example 0.1) are interpreted as due to either homogeneous sediments that are bioturbated afterwards, or structured sediments that are homogenized by bioturbation. The *H* index is not very sensitive in detection of variations in bioturbation intensity of strongly bioturbated samples (t4 fabric). For those samples, the range of variation of the *H* index is low, between -0.3 and 0.34.

The *H* method has numerous advantages over classical ichnofabric semiquantification: (1) laminated sediments are considered to reflect bottom-water anoxia, whereas massive non-laminated sediments reflect oxygenated bottom waters (Brodie and Kemp 1995). Nevertheless, laminae are reported in oxygenated environments with high sedimentation rates (Kuehl et al. 1988), and nonlaminated sediments may also arise in the absence of bioturbation or redeposition because of the steadiness of the sediment input (Grimm et al. 1996). Because no macroscopic fabric is visible in massive sediments, it is impossible to estimate bioturbation presence or absence using conventional methods. Applying the *H* method on homogeneous fabric, it is possible to distinguish between primary and bioturbated fabric. (2) Microbioturbation can be detected within laminae. *H* quantifies the intensity of such microbioturbation in laminated intervals. (3) A continuous record of bioturbation intensity is now available. (4) Quantification of bioturbation is done without subjectivity. (5) Measurements are performed on areas selected by the operator, e.g., at the lamina scale, as is the case for other image-analysis characterizations (Francus 1998). Therefore, the *H* method provides high-resolution analysis of hemipelagic sediments. The methodology is easy to implement: the necessary tools are a petrographic microscope or an electron microscope with image acquisition capabilities, basic calculations, and user-friendly, freeware image-analysis software.

Biases are potentially introduced because of undetected disturbance of the sediments, but this is also true for conventional semiquantified ichnofabric descriptions. The quality of the *H* index still needs to be assessed by laboratory experiments that take into account factors such as: type of bioturbation, microbial activity, cohesiveness of the sediment, and density currents. Other pertubating phenomena listed above should also be reproduced to control the ability of the methodology to detect them.

CONCLUSIONS

This paper presents the fundamentals of a powerful, easy-to-implement technique to quantify bioturbation. If careful selection of samples is made by macroscopic and microscopic examination to eliminate nonbiogenic perturbations, it is possible to quantify bioturbation using the *H* index, based on image-analysis measurements of hemipelagic sediment. *H* is low for bioturbated sediments and high for undisturbed and/or laminated sediments. The *H* index method is consistent with classical semiquantification schemes and is performed without subjectivity. The technique is more effective in the quantification of microbioturbation. The *H* index can be used to compare the intensity of bioturbation of similar fabrics in distant locations. Applying the *H* methodology should refine paleoecological reconstruction derived from key lacustrine and marine sequences and provide better results than previously achieved by semiquantitative scales.

ACKNOWLEDGMENTS

I thank E. Karabanov and M. Grachev for providing the samples, A. Lannoye and M. Bravin for technical assistance, and L. Anderson, P. Bart, F. Keimig, John Hubert, and John Southard for technical comments and smoothing of the English text. I'm also grateful to M. Droser, K. Grimm, S. Kuehl, and J. Macquaker for constructive review. This work has been supported by a Ph.D. valorization grant of the Université catholique de Louvain and the OSTC (Global Change Belgian Impulse program).

REFERENCES

Beck, Ch., Manalt, F., Chapron, E., Van Rensbergen, P., and De Batist, M., 1996, Enhanced seismicity in the early post-glacial period: evidence from the Post-Würm sediments of Lake Annecy, Northwestern Alps: Journal of Geodynamics, v. 22, p. 155–171.

Behl, R.J., and Kennett, J.P., 1996, Brief Interstadial events in the Santa Barbara basin, NE Pacific, during the past 60 kyr: Nature, v. 379, p. 243–246.

Bennett, R.H., Bryant, W.R., and Keller, G.H., 1981, Clay fabric of selected submarine sediments: fundamental properties and models: Journal of Sedimentary Petrology, v. 51, p. 217–232.

Brauer, A., and Negendank, J.F.W., 1993, Paleoenvironmental reconstruction of the late and postglacial sedimentary record of Lake Weinfelder Maar, *in* Negendank, J.F.W., and Zolitschka, B., eds., Paleolimnology of European Maar Lakes: Berlin, Springer-Verlag, Lecture Notes in Earth Sciences, v. 49, p. 223–236.

Bouabid, R., Nater, E.A., and Barak, P., 1992, Measurement of pore size distribution in a lamellar Bt horizon using epifluorescence microscopy and image analysis: Geoderma, v. 53, p. 309–328.

Brodie, I., and Kemp, A.E.S., 1994, Variation in biogenic and detrital fluxes and formation of laminae in late Quaternary sediments from the Peruvian coastal upwelling zone: Marine Geology, v. 116, p. 385–398.

Brodie, I., and Kemp, A.E.S., 1995, Pelletal structures in Peruvian upwelling sediments: Geological Society of London, Journal, v. 152, p. 141–150.

Chang, A.S., and Grimm, K.A., 1999, Speckled beds: Distinctive gravity-flow deposits in finely laminated diatomaceous sediments, Miocene Monterey Formation, California: Journal of Sedimentary Research, v. 69, p. 134–146.

Cheel, R.J., 1991, Grain fabric in hummocky cross-stratified storm beds: genetic implications: Journal of Sedimentary Petrology, v. 61, p. 102–110.

Droser, M.L., and Bottjer, D.J., 1986, A semiquantitative field classification of ichnofabric: Journal of Sedimentary Petrology, v. 56, p. 558–559.

Doyle, L.J., Carder, K.L., and Steward, R.G., 1983, The hydraulic equivalence of mica: Journal of Sedimentary Petrology, v. 53, p. 643–648.

Francus, P., 1998, An image-analysis technique to measure grain-size variation in thin-sections of soft clastic sediments: Sedimentary Geology, v. 121, p. 289–298.

Francus, P., and Karabanov, E., 2000, A computer-assisted thin-section study of lake Baikal sediments: a tool for understanding sedimentary processes and deciphering their climatic signal: International Journal of Earth Sciences, v. 89, p. 260–267.

Grimm, K.A., Lange, C.B., and Gill, A.S., 1996, Biological forcing of hemipelagic sedimentary laminae: Evidence from ODP site 893, Santa Barbara Basin, California: Journal of Sedimentary Research, v. 66, p. 613–624.

Grimm, K.A., and Orange, D.L., 1997, Synsedimentary fracturing, fluid migration, and subaqueous mass wasting: intrastratal microfractured zones in laminated diatomaceous sediments, Miocene Monterey formation, California, U.S.A: Journal of Sedimentary Research, v. 67, p. 601–613.

Hohman, R., Kipfer, R., Peeters, F., Piepke, G., Imboden, D.M., and Shimaraev, M.N., 1997, Processes of deep water renewal in Lake Baikal: Limnology and Oceanography, v. 42, p. 841–855.

Kennedy, S.K., and Mazzullo, J., 1991, Image-analysis method of grain size measurement, *in* Syvitski, J.P.M., ed., Principles, Methods, and Application of Particle Size Analysis: Cambridge, U.K., Cambridge University Press, p. 143–162.

Kennett, J.P., and Ingram, B.L., 1995, A 20,000-year record of ocean circulation and climate change from the Santa Barbara basin: Nature, v. 377, p. 510–514.

Krinsley, D.H., Pye, K., Boggs, S., and Tovey, N.K., 1998, Backscattered Scanning Electron Microscopy and Image Analysis of Sediments and Sedimentary Rocks: Cambridge, U.K., Cambridge University Press, 193 p.

Kuehl, S.A., Nittrouer, C.A., and DeMaster, D.J., 1988, Microfabric study of fine-grained sediments: observations from the Amazon subaqueous delta: Journal of Sedimentary Petrology, v. 58, p. 12–23.

Lamoureux, S., 1994, Embedding unfrozen lake sediments for thin-section preparation: Journal of Paleolimnology, v. 10, p. 141–146.

Lamoureux, S., 1999, Spatial and interannual variations in sedimentation patterns recorded in nonglacial varved sediments from the Canadian High Arctic: Journal of Paleolimnology, v. 21, p. 73–84.

Leroy, S.A.G., Giralt, S., Francus, P., and Seret, G., 1996, The high sensitivity of the palynological record in the Vico maar lacustrine sequence (Latium, Italy) highlights the climatic gradient through Europe for the last 90 ka: Quaternary Science Reviews, v. 15, p. 189–201.

Miller, M.F., and Smail, S.E., 1997, A semiquantitative field method for evaluating bioturbation on bedding planes: Palaios, v. 12, p. 391–396.

O'Brien, N.R., and Pietraszek-Mattner, S., 1998, Origin of the fabric of laminated fine-grained glaciolacustrine deposits: Journal of Sedimentary Research, v. 68, p. 832–840.

Pike, J., and Kemp, A.E.S., 1996, Preparation and analysis techniques for studies of laminated sediments, *in* Kemp, A.E.S., ed., Palaeoclimatology and Palaeoceanography from Laminated Sediments: Geological Society of London, Special Publication 116, p. 37–48.

Reineck, H.-E., and Singh, I.B., 1975, Depositional Sedimentary Environments: Berlin, Springer-Verlag, 439 p.

Russ, J.C., 1999, The Image Processing Handbook, 3rd Edition: Boca Raton, Florida, CRC Press, 771 p.

Savrda, C.E., 1995, Ichnologic applications in paleoceanographic, paleoclimatic, and sea-level studies: Palaios, v. 10, p. 565–577.

Savrda, C.E., Bottjer, D.J., and Gorsline, D.S., 1984, Development of a comprehensive oxygen-deficient marine biofacies model: evidence from Santa Monica, San Pedro, and Santa Barbara basins, California Continental Borderland: American Association of Petroleum Geologists, Bulletin, v. 68, p. 1179–1192.

Segall, M.P., and Kuehl, S.A., 1994, Sedimentary structures on the Bengal shelf: a multi-scale approach to sedimentary fabric interpretation: Sedimentary Geology, v. 93, p. 165–180.

Stow, D.A.V., and Bowen, A.J., 1980, A physical model for the transport and sorting of fine-grained sediment by turbidity currents: Sedimentology, v. 27, p. 31–46.

Taylor, A.M., and Gawthorpe, R.L., 1993, Application of sequence stratigraphy and trace

fossil analysis to reservoir description; examples from the Jurassic of the North Sea, *in* Parker J.R., ed., Petroleum Geology of Northwest Europe, Proceedings of the 4th Conference, p. 317–335.

VON MERKT, J., 1971, Zuverlässige Auszählungen von Jahresschichten in Seesedimenten mit Hilfe von Grob-Dünnschliffen: Archiv für Hydrobiologie, v. 69, p. 145–154.

WILKIN, R.T., BARNES, H.L., AND BRANTLEY, S.L., 1996, The size distribution of framboidal pyrite in modern sediments: An indicator of redox conditions: Geochimica et Cosmochimica Acta, v. 60, p. 3897–3912.

Received 10 September 1999; accepted 29 August 2000.

EFFECT OF MICA ON PARTICLE-SIZE ANALYSES USING THE LASER DIFFRACTION TECHNIQUE

SHAUN HAYTON,[1,2] CAMPBELL S. NELSON,[2] BRIAN D. RICKETTS,[2] STEVE COOKE,[3] AND MAURICE W. WEDD[4]

[1] *GeoSphere Exploration Ltd, P.O. Box 44285, Lower Hutt, Wellington, New Zealand*

[2] *Department of Earth Sciences, University of Waikato, Private Bag 3105, Hamilton, New Zealand*

[3] *School of Ocean and Earth Science, University of Southampton, Southampton SO14 3ZH, U.K.*

[4] *Malvern Instruments Ltd, Grovewood Road, Malvern, Worcestershire, WR14 1XZ, U.K.*

e-mail: shaun@geosphere.co.nz

ABSTRACT: **New sizing technologies commonly make particle-size analyses more routine, simpler, and less time consuming. The proliferation of new technologies led Syvitski et al. (1991) to recommend that ''new particle size instruments should no longer have their results compared with those of the classical methods of sieving and pipetting.'' However, care is required to ensure that results are broadly comparable to those obtained using established methodologies, especially where sediment classification and environmental processes are being interpreted using traditional schemes. The progressive development of new classification schemes based on modern particle-size analysis techniques will eventually mitigate this problem.**

Laser particle-size analyses of Upper Neogene micaceous terrigenous deposits from New Zealand have yielded some significantly different grain-size distributions compared to traditional sieving methods. These differences typically escalated with increasing sand content. A series of test samples spiked with increasing amounts of mica demonstrate that very small amounts of mica (< 2 wt%) have the potential to significantly alter the grain-size characteristics obtained using a laser particle sizer compared to sieve analyses. This is probably due to the mica particles having (a) a higher light-scattering property, and (b) large numbers of particles per unit volume, resulting in mica being overestimated.

INTRODUCTION

Grain size is a fundamental property of earth materials, relevant to their classification, origin, and geotechnical application. Grain size can be determined by a variety of techniques, including sieving, sedimentation, electrozone sensing, microscopy, and laser diffraction, each of which defines the size of a particle in a different way by measuring different properties of the same material (McManus 1988; Syvitski et al. 1991). In recent years, laser diffraction size analysis has become a popular technique because it is rapid, is highly reproducible, and covers a spectrum of clay- to sand-size grades (e.g., Agrawal et al. 1991; Konert and Vandenberghe 1997).

Laser diffraction analysis is based on the principle that particles of a given size diffract light through an angle that increases with decreasing particle size. When monochromatic light is passed through a suspension, the diffracted light is focused onto a multi-element ring detector that senses the angular distribution of scattered light. This scattered light distribution is then converted into a distribution of spherical particles that would produce the observed scattering intensity pattern (McCave and Syvitski 1991).

In a comprehensive sedimentological study involving the routine laser diffraction analysis of more than 600 samples of Pliocene sandstones and mudstones from Wanganui basin, North Island, New Zealand (Hayton 1998), our Malvern Mastersizer-S instrument (long bed version 2.14, 300 mm lens, analysis range from -1 to 15 ϕ) commonly yielded lower sand contents in samples than values previously obtained by sieve analysis on the same samples. In general the divergence between the two sets of results increased with increasing sand content (Fig. 1). The apparent discrepancy was unexpected because the particle-size distributions of a variety of sedimentary, soil, and pyroclastic materials analyzed using the laser diffraction technique during other studies gave results that were consistent to within a few percent of those obtained using traditional sizing techniques.

The Pliocene sediments in this study differ from most of the previously analyzed deposits because they are distinctly micaceous (up to 5%). We hypothesized that underestimation of the content of sand in our samples related somehow to the sheet-like nature of the mica grains wherein the dimension of the principal crystallographic *c* axis may be several times smaller than the other axes, resulting in a significantly reduced equivalent-size sphere and thus diminished sand concentration. In an attempt to understand what role mica might play in causing the divergence of results between the laser- and sieve-derived data, a series of analyses was conducted using quartzofeldspathic sand spiked with increasing amounts of sand-size mica.

TEST ANALYSES

A known weight of clean, nonmicaceous, fine- to medium-grained quartzofeldspathic beach sand was run through the laser system, providing baseline particle-size results (Fig. 2). Small amounts (wt%) of mica (mixture of biotite and muscovite), previously sieved to a size range of 2–4 ϕ, were progressively added to the beach sand, and repeat laser analyses undertaken at each step (Table 1). A sample consisting of 100% mica was also analyzed.

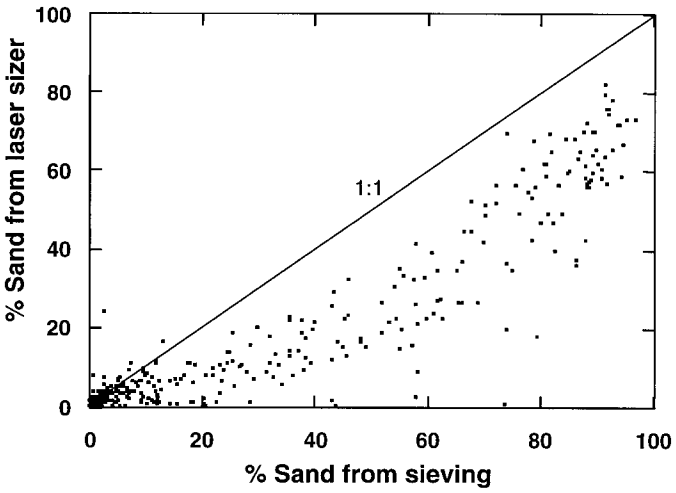

FIG. 1.—Cross-plot of sand percentages obtained using wet sieving and laser particle size techniques (no. of samples = 372). Data from Hayton (1998).

 1073-130X/01/071-507/$03.00

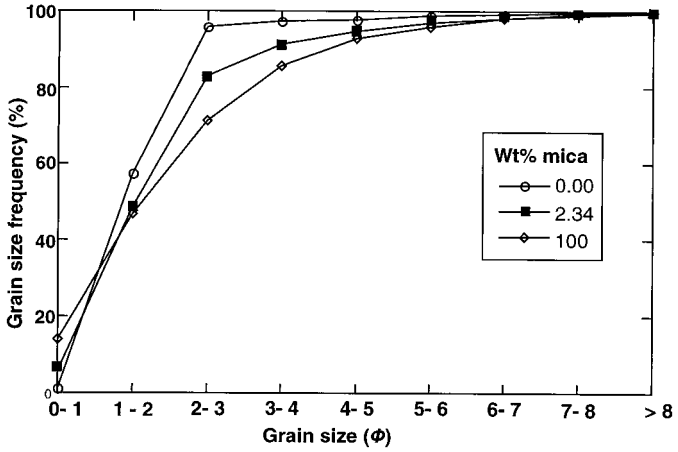

FIG. 2.—Change in cumulative frequency curves for pure quartzofeldspathic sand (0 wt% mica), pure mica (100% mica), and a sample containing 2.34 wt% of mica.

Given the laser obscuration tolerances inherent in all laser particle-size analyzers, this series of analyses was undertaken in two parts separated at 9.09 wt% mica, with this sample run being repeated in both sets and reported in Table 1 as the average of the two analyses. The 100% mica test was a third, separate analysis. Flocculation problems, as noted by Konert and Vandenberghe (1997), were not encountered given the absence of clay material and the short time over which the experiments were undertaken. Equipment testing with certified reference materials indicated that local water supplies were suitable for the day-to-day grain-size analyses performed on our instrument, rather than the degassed and deionized water used by Loizeau et al. (1994) and Konert and Vandenberghe (1997). In our experiments, degassing of the suspension is not likely to be a problem because the pump and stirrer were used continuously in the sample chamber.

To determine the effect of the addition of mica, the weighted average percentage change was determined for each of the mica-bearing sand records as follows (see worked example in Table 2 and Fig. 2):

(a) For each particle-size range, the absolute change in concentration between the pure sand (S) and mica curves (M) was determined, giving total possible change W (an absolute value), where W = S-M.

(b) The grain-size concentration change from pure sand (S) to the sand and mica curve (X) was resolved, and expressed as a percentage of total possible change Y, where

$$Y = ([S - X]/W)100.$$

TABLE 1.—*Laser sizer results of the mica test series where 2–4 ϕ sieved mica was progressively introduced into a clean non-micaceous beach sand. The elongated nature of many of the mica particles means that grains coarser than 2 ϕ are measured by the laser sizer.*

Wt% Mica Added	Grain Size (ϕ)								
	0–1	1–2	2–3	3–4	4–5	5–6	6–7	7–8	>8
0	1.01	56.22	38.58	1.63	0.47	0.88	0.46	0.52	0.22
0.40	2.85	52.42	37.06	2.86	1.14	1.57	0.95	0.76	0.39
0.79	3.97	49.58	36.56	3.94	1.71	1.87	1.09	0.80	0.50
1.19	4.94	48.41	35.69	4.53	2.08	1.91	1.11	0.82	0.50
1.57	4.39	46.67	35.55	5.76	2.47	2.12	1.21	0.79	1.06
1.96	4.77	46.25	34.95	6.13	2.71	2.16	1.20	0.78	1.04
2.34	5.58	43.11	34.43	8.40	3.35	2.17	1.21	0.77	1.01
3.85	8.15	39.61	31.84	10.16	4.39	2.50	1.43	0.86	1.03
5.66	8.77	36.75	30.35	11.99	5.67	2.95	1.67	0.98	0.85
7.41	10.79	35.06	28.73	12.46	6.08	3.11	1.82	1.06	0.86
9.09	11.43	35.35	27.61	12.65	6.22	3.03	1.81	1.06	0.84
13.04	12.59	35.01	26.62	12.84	6.31	2.97	1.78	1.01	0.80
16.67	12.04	33.95	26.62	13.53	6.73	3.18	1.95	1.12	0.86
20.00	12.11	33.59	26.29	13.72	6.92	3.29	2.01	1.16	0.89
23.08	12.30	33.24	26.06	13.88	7.04	3.36	2.06	1.20	0.93
100.00	13.84	32.91	24.78	14.17	7.11	3.24	1.99	1.12	0.83

TABLE 2.—*Worked example for establishing the weighted average percentage change values. The cumulative frequency curve for the mica concentration used in this worked example (2.34 wt%) is shown in Figure 2.*

Size Class (ϕ)	Pure Sand (S)	Pure Mica (M)	Total Possible Change (W)	Mica Content (2.34 wt%) (X)	Percentage of Possible Change (%) (Y)	Weighted Percentage Change (%) (Z)
0–1	1.01	13.84	12.83	5.58	35.6	1.98
1–2	56.22	32.91	23.31	43.11	56.2	24.2
2–3	38.58	24.78	13.80	34.43	30.1	10.4
3–4	1.63	14.17	12.54	8.40	54.0	4.5
4–5	0.47	7.11	6.64	3.35	43.4	1.5
5–6	0.88	3.24	2.36	2.17	54.7	1.2
6–7	0.46	1.99	1.53	1.21	49.0	0.6
7–8	0.52	1.12	0.60	0.77	41.7	0.3
>8	0.22	0.83	0.61	1.01	129	1.3
Weighted average percentage change						46

(c) The percentage of total possible change was weighted (Z) according to the weight percent of sample in each grain size, where Z = Y·X%.

(d) The weighted percentage change values for each particle size (Z) were summed to give the weighted average percentage change from the pure sand to the mica-bearing curves.

Using this approach it is evident that the effect of adding mica has been to force the grain-size curve towards that of the pure mica to an extent far in excess of the actual concentration of mica. Figure 3 plots the weighted average percentage change between the starting quartzofeldspathic beach sand curve and the mica-bearing curves at each concentration step, and highlights the very rapid shift towards the pure mica endpoint. This shift is so dramatic that only 2.5 wt% of mica gives a predominantly mica-based grain-size distribution rather than a total sediment distribution.

DISCUSSION AND CONCLUSIONS

What causes the presence of mica to bias the laser particle-size results to such an extent? Because the total scattered light is proportional to the total number of particles in the measurement cell and their combined scattering cross section, the answer probably lies in the number of particles in the quartzofeldspathic sand and mica fractions and their relative cross-sectional areas. The shape of mica particles means that a unit weight of mica will generate significantly more particles than the same unit weight of quartzofeldspathic sand. Thus significantly less mica (wt%) is required to obtain the same number of particles as in a much larger amount (wt%) of quartzofeldspathic sand. In terms of cross-sectional area, the two-di-

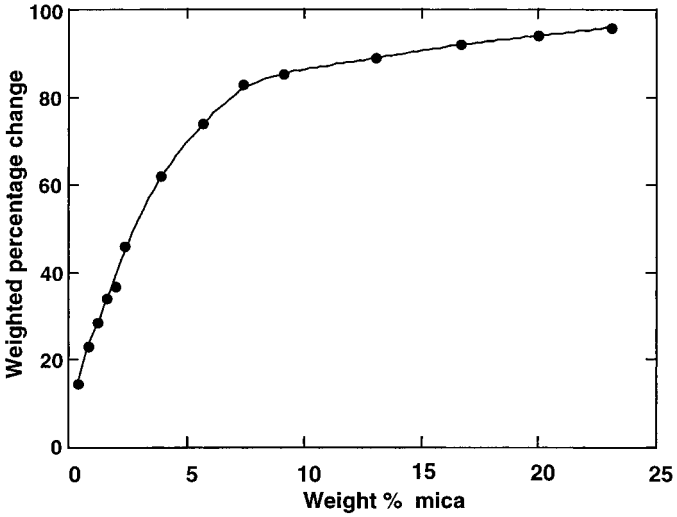

FIG. 3.—Plot showing the relationship between the wt% mica and the degree of change produced (weighted average percentage change; sum of Z e.g., see Table 2 for example where 2.34 wt% of added mica).

mensional nature of the mica particles will result in a much greater percentage of the scattering in a laser diffraction particle sizer, and so they are overestimated in terms of their volume.

Particle-size analysis is undertaken so that materials can be compared to any of a number of established classification schemes, for example textural classification triplots (Folk 1954), degrees of sorting (Folk and Ward 1957; Friedman and Sanders 1978), and two-component grain-size variation diagrams (Friedman 1961, 1967, 1979). For the case of new particle-size analysis technologies, in particular laser analyzers, some of the basic assumptions such as spherical geometry and uniform mineralogy of detrital grains need to be carefully examined before comparisons with traditional grain-size analyses can be made. Our analysis of micaceous, quartzofeldspathic sandstones illustrates the potential difficulties in making such comparisons. In this case the results indicate that care needs to be taken in interpreting the laser sizer textural data because even very small quantities of mica and mica-like minerals can have a significant effect on the particle size distribution (Fig. 3). Whether or not an analogous mica-clay problem exists for finer-grained sediments remains to be determined.

ACKNOWLEDGMENTS

We are very grateful to J.-L. Loizeau, an anonymous reviewer, and G.M. Ashley for their helpful comments about this paper.

REFERENCES

Agrawal, Y.C., McCave, I.N., and Riley, J.B., 1991, Laser diffraction size analysis, *in* Syvitski, J.P.M., ed., Principles, Methods and Applications of Particle Size Analysis: New York, Cambridge University Press, p. 119–128.

Folk, R.L., 1954, The distinction between grain size and mineral composition in sedimentary rock nomenclature: Journal of Geology, v. 62, p. 344–359.

Folk, R.L., and Ward, W.C., 1957, Brazos River bar: A study in the significance of grain-size parameters: Journal of Sedimentary Petrology, v. 27, p. 3–26.

Friedman, G.M., 1961, Distinction between dune, beach, and river sands from textural characteristics: Journal of Sedimentary Petrology, v. 31, p. 514–529.

Friedman, G.M., 1967, Dynamic processes and statistical parameters compared for size frequency distribution of beach and river sands: Journal of Sedimentary Petrology, v. 37, p. 327–354.

Friedman, G.M., 1979, Address of the retiring president of the International Association of Sedimentologists: Differences in size distributions of populations of particles among sands of various origins: Sedimentology, v. 26, p. 3–32.

Friedman, G.M., and Sanders, J.E., 1978, Principles of Sedimentology: New York, John Wiley and Sons Inc., 792 p.

Hayton, S., 1998, Sequence stratigraphic, paleoenvironmental, and chronological analysis of the late Neogene Wanganui River section, Wanganui basin [unpublished Ph.D. thesis]: University of Waikato, Hamilton, 201 p.

Konert, M., and Vandenberghe, J., 1997, Comparison of laser grain size analysis with pipette and sieve analysis: a solution for the underestimation of the clay fraction: Sedimentology, v. 44, p. 523–535.

Loizeau, J.L., Arbouille, D., Santiago, S., and Vernet, J.P., 1994, Evaluation of a wide range laser diffraction grain size analyzer for use with sediments: Sedimentology, v. 41, p. 353–361.

McCave, I.N., and Syvitski, J.P.M., 1991, Principles and methods of geological particle size analysis, *in* Syvitski, J.P.M., ed., Principles, Methods and Applications of Particle Size Analysis: New York, Cambridge University Press, p. 3–21.

McManus, J., 1988, Grain size determination and interpretation, *in* Tucker, M., ed., Techniques in Sedimentology: Oxford, U.K., Blackwell Scientific Publications, p. 63–85.

Syvitski, J.P.M., LeBlank, K.W.G., and Asprey, K.W., 1991, Interlaboratory, interinstrument calibration experiment, *in* Syvitski, J.P.M., ed., Principles, Methods and Applications of Particle Size Analysis: New York, Cambridge University Press, p. 174–193.

Received 27 October 1999; accepted 22 October 2000.

AN INTEGRATED CATHODOLUMINESCENCE VIDEO-CAPTURE MICROSAMPLING SYSTEM

BRUCE W. FOUKE[1] AND JOHN RAKOVAN[2]

[1] *Department of Geology, University of Illinois, 1301 W. Green Street, Urbana, Illinois 61801, U.S.A.*
e-mail: fouke@uiuc.edu

[2] *Department of Geology, Miami University, Oxford, Ohio 45056, U.S.A.*

Abstract: A new system is described that permits real-time microdrilling of sedimentary grains and crystals within cathodoluminescence zonations. Low-light cathodoluminescence photomicrograph images are captured with a thermoelectrically cooled color video camera and saved on a computer. These cathodoluminescence images are then transparently superimposed on a standard color video image of the sample being microdrilled on a 20 μm scale using a video mixer. This integrated system can be applied to a wide variety of sedimentary rocks and minerals.

INTRODUCTION

The advent of inexpensive high-resolution digital cameras has revolutionized standard techniques in microscope image acquisition. This is particularly true when computer-based digital image manipulation is desired for both qualitative and quantitative applications. The recent development of cooled digital cameras allows for quick and precise image capture even under extremely low light conditions such as during cathodoluminescence (CL) microscopy. This paper presents a new low-cost integrated system that utilizes cooled digital cameras for the rapid color acquisition of low-light CL photomicrograph images. These high-resolution digital images are then used as a map within which real-time microdrilling is done on a 20 micrometer scale to extract sample powders for geochemical analyses. While the geological applications are numerous, this system has been specifically designed for paleoenvironmental reconstructions from carbonate deposits. CL petrography and microsampling are two essential tools in many types of sedimentary geochemistry studies, and new means are continually being sought to increase the efficiency, accuracy, and spatial resolution of these techniques.

CL PETROGRAPHY AND DIGITAL IMAGING

CL, defined as the emission of light from a sample during electron bombardment, is a technique that has been used to study trace-element chemistry and zoning in minerals such as calcite (Paquette and Reeder 1990; Reeder 1991), dolomite (Searle 1990; Fouke and Reeder 1992); zircon (Hanchar and Rudnick 1995), apatite (Mariano 1988; Rakovan and Reeder 1994), diamond (Davies 1979), feldspar (Finch and Klein 1999; Goetz et al. 1999), quartz (Zinkernagel 1978; Onasch and Venneman 1995), and many others. Furthermore, the combination of plane-light (PL) and CL petrography has proven to be an invaluable tool with which to interpret the depositional and diagenetic history of sedimentary rocks (Marshall 1988; Barker and Kopp 1991). It is in these studies of sedimentary minerals and rocks that CL has seen its widest application in the earth sciences.

Depending on the type of sample being analyzed, CL may be produced over a wide range of wavelengths from ultraviolet to infrared (Marshall 1988). Because of reductions in light during transmission through vacuum chamber windows and microscope optical systems, the visible spectrum of CL is the range most commonly used (350–850 nm; Machel and Burton

 1073-130X/01/071-509/$03.00

1991). Until recently, CL analyses completed on stand-alone petrographic microscopes have relied on standard photographic techniques using 35-mm film for image recording. This technique has required long exposure times (tens of seconds to several minutes), removing unnecessary optical elements from the microscope and use of low-magnification objectives so that enough light reaches the film, and analysis of minerals with relatively strong CL emissions. These factors have prevented the analysis and photography of many dim CL mineral samples and have generated significant controversy over the interpretation of CL emission patterns (Machel et al. 1991; Habermann et al. 1998; Bruhn and Bruckshen 1999). Until recently, color video capture of low-intensity CL was not possible because of thermally induced charges, known as ''dark charge,'' on the surface of standard CCD video chips (Spring 2000). These thermal effects significantly reduce resolution by creating a noisy image during photon capture and prevent long exposure times.

To minimize the effect of dark charge, CCD cameras are cooled to increase their quantum efficiency. This reduces the necessary exposure time for a given light level while decreasing the dark charge. Two different methods of CCD cooling are available (see review in Spring 2000); liquid nitrogen and thermoelectric (Peltier). For applications where maximum CCD cooling is necessary, liquid nitrogen methods are still commonly used. For most photomicrograph applications, however, Peltier cooling is adequate and eliminates the drawback of having to constantly refill nitrogen cooled cameras. In addition to cooling, numerous other factors affect performance in low-light conditions. Several are essential to consider when choosing a CCD camera for CL photography. These include format and resolution, spectral response, the mechanism of color reproduction, grade, and the allowed exposure time (Inoue and Spring 1997; Spring 2000).

The scientific digital camera market is rapidly evolving. Until recently, CCDs have been the most popular device for digital image capture. Another new technique, complementary metal oxide semiconductor (CMOS), is quickly gaining favor over CCD technology and may surpass it in the near future. Because of susceptibility to noise in CMOS detectors, CCDs currently excel at low-light image capture. There are currently many manufacturers of cooled CCD cameras that are appropriate for CL image collection. Dramatic changes in cost and technology occur frequently. The authors tested several commercial cooled CCD cameras ranging in price from $6,000 to $15,000, including the RS Photometrics Coolsnap, the Diagnostic Instruments SPOT, the Princeton Instruments PentaMAX, and the Optronics DEI-750T. Each had its own unique characteristics but all were found to be quite good at accurate digital image capture under conditions of low CL. For reasons described below, the Optronics DEI-750T camera was chosen for this integrated CL-microsampling system.

MICROSAMPLING

Microsampling techniques using small diamond-coated drill burrs to extract powder from carbonate minerals for isotopic analyses were first described by Prezbindowski (1980). Dettman and Lohmann (1995) advanced the spatial resolution of microdrilling techniques (also termed *micromilling*) for carbonates to 20 μm, as well as developed the mass spectrometry techniques required for analyzing the small volumes of sample powder that are extracted. The minimum sample size of extracted carbonate powder required for gas ratio mass spectrometry is approximately 0.1 μmole or 10 μg (Dettman and Lohmann 1995). The Dettman and Lohmann (1995) micromilling technique relies on digitizing CL photomicrographs taken with standard 35 mm film and using these images as maps within which computerized stepping motors position the spinning drill burr. A computer program to provide additional spatial control of the Dettman and Lohmann (1995) micromilling system is presented by Wurster et al. (1999). Although a well established and proven technique, the approach is limited in that the precise placement of the microdrill within CL-defined crystal zones is done by stepping motors rather than direct visual manipulation. The Dettman and Lohmann (1995) approach is also useful with other microdrilling and *in situ* isotopic analyses of carbonates, including: (1) electro-freezing microtome (Wada 1988), (2) laser ablation (LASSIE; Smalley et al. 1989; Fouke et al. 1996a), (3) secondary ion mass spectrometry (SIMS; Leshin et al. 1999), and 4) inductively coupled plasma mass spectroscopy (ICP-MS; Land et al. 1997). However, the instrumentation for these techniques is not commonly available, expensive to use, problems exist with standards and reproducibility, and accurate spatial control of the analysis spot in a CL map is often difficult or not possible.

The integrated CL video-capture microsampling system described in this paper capitalizes on the efficiency and speed of cooled CCD video chip technology. The superior 20 μm spatial resolution of microdrilling (Dettman and Lohmann 1995) is retained, while permitting direct visual real-time placement of the spinning drill burr within CL crystal growth zones. Use of the cooled CCD camera also allows standard PL and CL petrography and screening analyses to be done quickly and independently from microdrilling. As an example, images requiring 20 seconds to 2.5 minutes of exposure with 400 ASA 35 mm film and the CL instrument operating at 500 μA and 10 kV, now require 0.1 to 5 seconds at the same CL operating conditions using the cooled CCD camera. This creates a high-resolution CL image file that is immediately available for use. Additional attractive aspects of the integrated system described herein is it is relatively inexpensive to build and easy to maintain.

DESCRIPTION OF SYSTEM

The real-time integration needed for the operation of this system requires that CL digital images collected with the cooled CCD camera from the CL microscope stage be overlaid on a real-time video signal collected from a normal CCD camera on the microsampling stage. The microdrill must be precisely placed in compositional zonations observed only under CL petrography. This overlay can be achieved in two ways. The first is using a video mixing board that combines the video signals from the cameras on the CL stage and the microdrilling stage, respectively. The second is by using computer software that is capable of combining direct digital signals that are constantly being refreshed from digital cameras on the CL stage and the microdrilling stage. Given the current price of computer imaging technologies and the ubiquity of video camera applications, it is currently most simple and cost effective to choose the video signal option and combine the video feeds on a mixing board. This is the technique chosen for the system described in this article. The primary drawback to this video technique is that image resolution is decreased in the signal conversion from digital to analog. As direct digital instrumentation becomes more popular on the commercial market, digital mixing will eventually become as convenient and cost effective as video mixing.

Of the cooled color CCD cameras tested in this study, the Optronics DEI-750T was chosen because it offered the highest-resolution video output. The Optronics DEI-750T camera is electronically cooled to 30° C below ambient air temperature, allowing for exposure times of up to two minutes with minimal dark charge. Its resolution is 768(H) $\times$ 494(W) pixels, allowing direct production of publication-quality color and black-and-white photographic enlargements up to 8 cm in diameter from standard desktop inkjet printers. Enlargements of greater size are noticeably pixilated, yet of high enough quality for use in conference posters and other applications.

CL Video Capture

A schematic diagram and photograph of the CL video-capture microsampling system is presented in Figure 1. A detailed list of the manufacturer names, addresses, and specific part numbers is available from the authors. The system is built on a low-vibration table in a room that can be completely darkened and kept as dust free as possible. A cold cathode CL vacuum stage

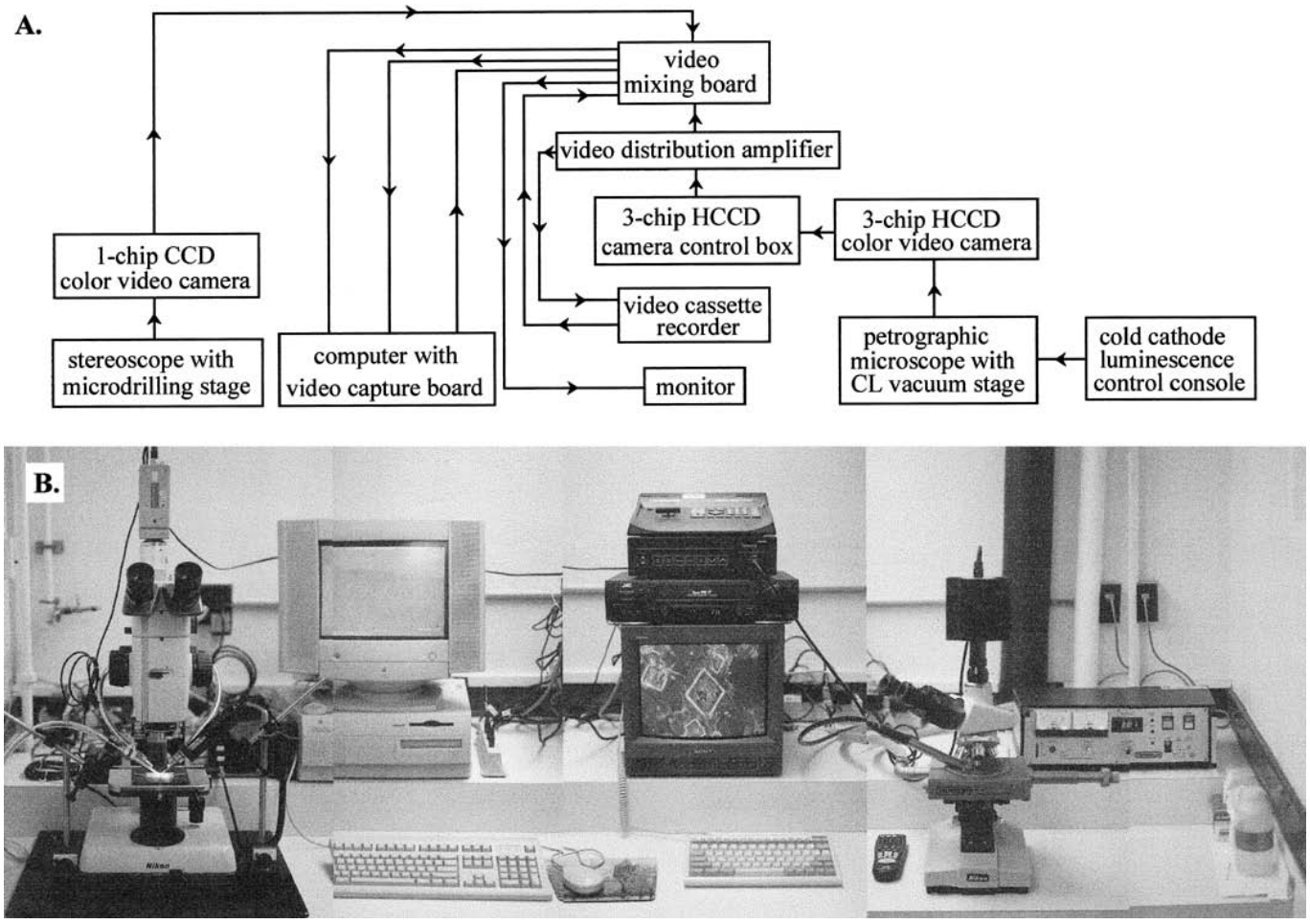

FIG. 1.—**A)** Schematic diagram and **B)** photographic mosaic of the integrated cathodoluminescence video-capture microdrilling system.

is attached to a research-grade petrographic microscope. The thermoelectrically cooled CCD video camera is mounted on the microscope's trinocular head with a standard C-mount fitting to capture the CL. The phototube provided with the camera contains an adjustment ring to precisely synchronize the video camera magnification and focus with the image observed through the microscope eyepieces. The CL image video signal from the cooled CCD camera is then split, with one line routed into a video mixing board and the other line fed into a conventional video cassette recorder (VCR). From the mixing board the CL image signal is then routed into a computer via a video capture board that translates it from video into digital format. Computer software provided with the video capture board is then used to transfer the digital images to photographic or image-analysis programs. The video capture board requires an external monitor on which the PL and CL image capture and manipulation is completed.

Microdrilling

The microdrilling assembly consists of two parts. The first is a 2-cm-thick steel plate on which a stereoscopic microscope is mounted. The weight of the plate reduces vibration and provides a platform on which movable electromagnetic bases suspending the microdrilling and vacuum assemblies can be anchored. The microdrilling assembly is a standard low-speed handset dental drill attached to a manual X-Y-Z micromanipulator with a custom-designed aluminum bracket (Fig. 2A). The drill (UPower Laboratory Hand Engine manufactured by Brasseler USA) accepts a large range of drill-bit shank sizes and shapes (up to 4 mm in diameter) and has a variable speed control from 100 to 100,000 rpm. Drill bits composed of high-speed cobalt steel with a diamond powder coating can be purchased with tip sizes as small as 12 μm in diameter (scriber burrs manufactured by Brasseler U.S.A.). The vacuum assembly consists of a custom-designed bracket that removes sample powder with glass fiber filters (0.2 to 0.6 μm mesh) from a vacuum line through a micropipette tip (Fig. 2A). Prior to collecting each new sample the pipette tips are replaced and the aluminum clamp is blown clean with compressed air. The drilled powders are collected on glass filters that mount behind micropipette tips that are held in place by suction from the vacuum pump. The stereoscope has a standard ceramic rectangular stage with X-Y manual controls. The combination of the X-Y-Z micromanipulators and the X-Y mechanical microscope stage permit precise placement of the microdrill and vacuum system on the thin section or rock chip. A 1-chip CCD color video camera is attached to the trinocular head of the stereoscope, and video images are fed directly through the video mixing board and into the computer via the video capture board (Fig. 1). A bifurcating fiber-optic light source is used to illuminate the surface of the sample being drilled. The resulting integrated system allows accurate real-time positioning of the slowly spinning microdrill burr tip overlaid by a transparent CL image.

OPERATING PROCEDURE

Sample Preparation

Thin sections as well as rock chips of various sizes and shapes can be analyzed using this system. The CL stage is equipped with an aluminum

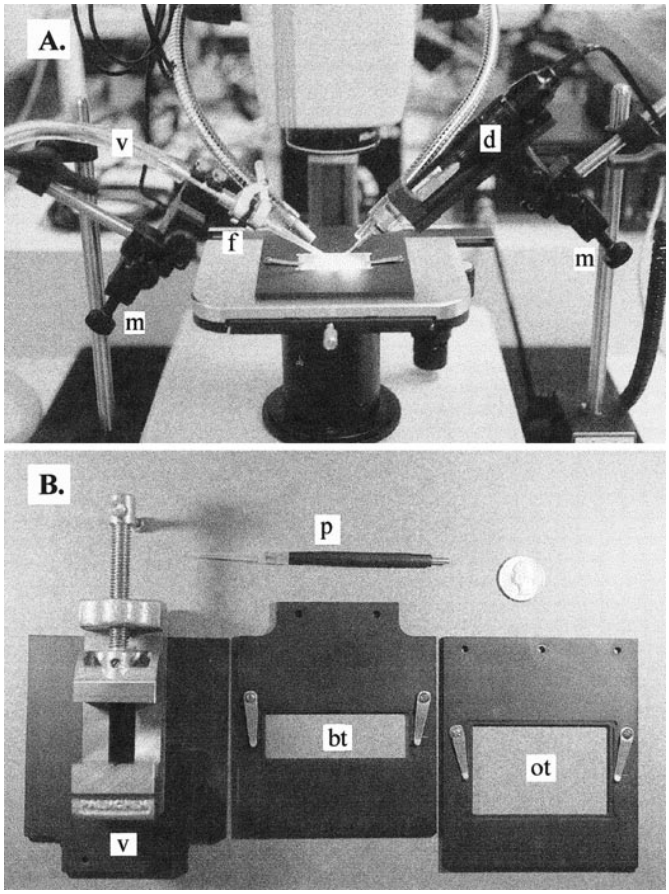

FIG. 2.—Photographs of the **A)** microdrilling stage and **B)** custom-made accessories. Lettering in part A designates the microdrill (d), X-Y-Z micromanipulators (m), vacuum-line (v), and the vacuum line filter holder (f). Lettering in part B represents the pipette-tip extension (p), vise (v), holder for biological thin sections (bt), and holder for oversized thin sections (ot).

mount that will accommodate petrographic (2.7 cm × 4.6 cm), standard biological (2.5 cm × 7.5 cm), and oversize (7.5 cm × 0.5 cm) thin sections. A high-quality polish on the thin sections and rock chips is required for the best optical resolution. Custom aluminum mounts and a small vise have been made for the microdrilling stage to hold the petrographic, standard biological, and oversize thin sections (Fig. 2). Sample impregnation and the adhesion of rock chips to glass thin-section slides should be done with a high-heat-resistant epoxy specifically recommended for CL analyses.

CL Image Capture

The computer video capture program and the video mixing board are electronically switched to receive the signal from the cooled CCD color video camera on the petrographic microscope with the CL stage (Fig. 1). A set of paired PL and CL images are collected and saved on the computer hard drive as well as on videotape. Each high-resolution digital image is approximately 1.1 Mb. Collection, manipulation, and storage of several images simultaneously can be completed on any computer with standard hard drive (multiple Gb's) and RAM (> 64 Mb) capabilities.

Microsample Powder Collection

The thin section or rock chip is then removed from the CL stage vacuum chamber and transferred to the microdrilling stage. The computer video capture program and the video mixing board are switched to receive the

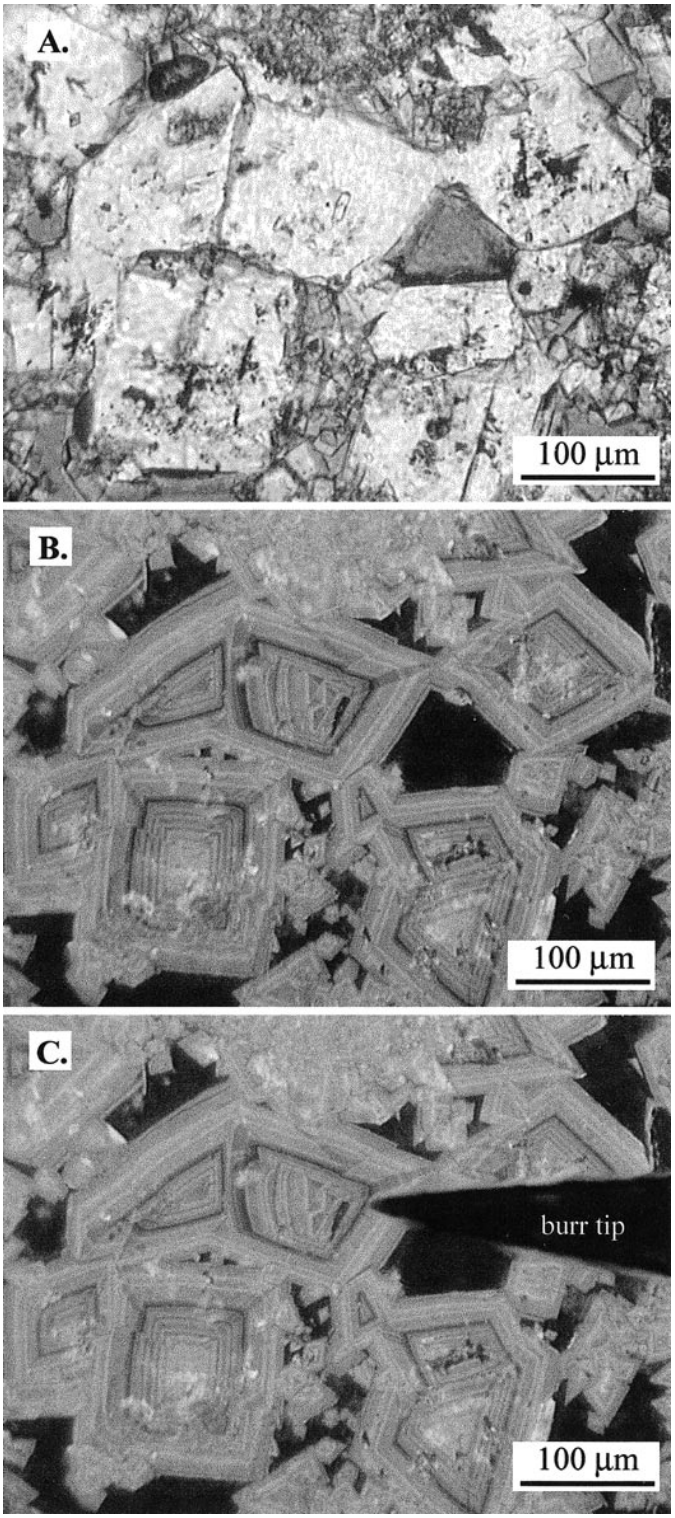

FIG. 3.—**A, B)** Paired plane-light and cathodoluminescence photomicrograph images of Dolomite I' from the Seroe Domi Formation. **C)** Overlay of the transparent CL image in part B on a real-time PL video image of the spinning drill burr tip (labeled). Note that the drill tip has not yet begun drilling into the sample in the photograph, and appears as a triangular dark non-CL region.

signal from the standard color CCD video camera on the stereoscope with the microdrilling stage (Fig. 1). Once the field of view and magnification are adjusted, the CL image is overlaid on the real-time video signal of the spinning drill burr on the microdrilling stage using the video mixing board. Precise superpositioning of the CL image over the PL image is done using three or more registration marks that are drilled on the sample surface. In real-time mode, the drill burr is positioned manually within the CL image map.

The microsampled powders can be removed using a variety of techniques, one of these being the vacuum system described above. After collection and with the vacuum off, the glass filter is then carefully removed with tweezers from the aluminum bracket and placed into clean glass or stainless steel reaction vials that can be loaded directly onto the mass spectrometer. An alternative method is to remove the powder from the sample surface with a clean scalpel blade. Processing of the sample powder will then follow the procedures of the particular laboratory being used for the analyses.

APPLICATION EXAMPLE

Neogene marine limestones of the Seroe Domi Formation on the island of Curaçao, Netherlands Antilles, have experienced three major episodes of dolomitization (Fouke and Reeder 1992; Fouke, 1994; Fouke et al. 1996b). Large euhedral dolomite crystals with distinct CL zonations precipitated during the Middle Miocene (Dolomite I), Late Miocene (Dolomite I'), and Early Pliocene (Dolomite II; Fig. 3). Figures 3A and B are paired PL and CL photomicrograph images of Dolomite I' collected using the CL video-capture system described in this paper. Figure 3C is a view of the transparent CL image overlaid on a real-time video image of the spinning drill burr tip. The vacuum pipette tip is placed directly over the drill tip during powder collection (Fig. 2A).

SUMMARY

This paper describes an integrated system in which CL is collected from the surface of a polished rock sample and fed directly into a computer via a thermoelectrically cooled video camera. Samples are removed from the CL vacuum stage and microdrilled while being photographed with a standard color video camera. The previously captured CL image is then superimposed as a transparency over the real-time microdrilling video feed using a video mixer. Microdrilled sample powders for elemental and isotopic chemical analyses are collected with a vacuum system onto glass filters or using a scalpel. This system is applicable to a wide variety of mineral and rock types.

ACKNOWLEDGMENTS

This work was supported by grants to B. Fouke from the Department of Geology at the University of Illinois Urbana-Champaign, the University of Illinois Critical Research Initiative, and The Petroleum Research Fund administered by the American Chemical Society. Editorial reviews by S. Boggs, K. Milliken, D. Marshall, J. Southard, and an anonymous reviewer are gratefully acknowledged. The authors would like express their sincere thanks to A. Vitous (Fryer Company) for his guidance in helping to develop the video acquisition system, and to J. VanDeventer and S. Baker (University of Illinois School of Life Sciences Machine Shop) for their skill in custom manufacturing the microdrilling platform and vacuum components.

REFERENCES

Barker, C.E., and Kopp, O.C., 1991, Luminescence Microscopy and Spectroscopy: Qualitative and Quantitative Applications: SEPM Short Course 25, 195 p.

Bruhn, F., and Bruckschen, P., 1999, Low limit of Mn^{2+}-activated cathodoluminescence in calcite: state of the art—Discussion: Sedimentary Geology, v. 123, p. 147–148.

Davies, G., 1979, Cathodoluminescence, *in* Field, J.E., ed., Properties of Diamond: London, Academic Press, p. 165–181.

Dettman, D.L., and Lohmann, K.C., 1995, Microsampling carbonates for stable isotope and minor element analysis: physical separation on a 20 micrometer scale: Journal of Sedimentary Research, v. A65, p. 566–569.

Finch, A.A., and Klein, J., 1999, The causes and petrological significance of cathodoluminescence emissions from alkali feldspars: Contributions to Mineralogy and Petrology, v. 135, p. 234–243.

Fouke, B.W., 1994, Deposition, Diagenesis and Dolomitization of Neogene Seroe Domi Formation Coral Reef Limestones on Curaçao, Netherlands Antilles: The Hague, Foundation for Scientific Research in the Caribbean Region, Publications, v. 135, 197 p.

Fouke, B.W., and Reeder, R.J., 1992, Surface structural controls on dolomite composition: Evidence from sectoral zoning: Geochimica et Cosmochimica Acta, v. 56, p. 4015–4024.

Fouke, B.W., Everts, A.-J.W., Zwart, E.W., Schlager, W., Smalley, P.C., and Weissert, H., 1996a, Subaerial exposure unconformities on the Vercors carbonate platform (SE France) and their sequence stratigraphic significance, *in* Howell, J.A., and Aitken, J.F., eds., High Resolution Sequence Stratigraphy: Innovations and Applications: Geological Society of London, Special Publication No. 104, p. 295–320.

Fouke, B.W., Meyers, W.J., Hanson, G.N., and Beets, C.J., 1996b, Chronostratigraphy and dolomitization of the Seroe Domi Formation, Curaçao, Netherlands Antilles: Facies, v. 35, p. 293–320.

Goetz, J., Habermann, D., Neuser, R.D., and Richter, D.K., 1999, High-resolution spectrometric analysis of rare earth elements—activated cathodoluminescence in feldspar minerals: Chemical Geology, v. 153, p. 81–91.

Habermann, D., Neuser, R.D., and Richter, D.K., 1998, Low limit of Mn^{2+}-activated cathodoluminescence in calcite: state of the art: Sedimentary Geology, v. 116., p. 149–151.

Hanchar, J.M., and Rudnick, R.L., 1995, Revealing hidden structures; the application of cathodoluminescence and back-scattered electron imaging to dating zircons from lower crustal xenoliths: Lithos, v. 36, p. 289–303.

Inoue, S., and Spring, K.R., 1997, Video: The Fundamentals: New York, Plenum Press, 197 p.

Land, L.S., Mack, L.E., Milliken, K.L., and Lynch, L.F., 1997, Burial diagenesis of argillaceous sediment, South Texas Gulf of Mexico sedimentary basin: a reexamination: Geological Society of America, Bulletin, v. 109, p. 2–15.

Leshin, L.A., McKeegan, K.D., Carpenter, P.K., and Harvey, R.P., 1999, Oxygen isotopic constraints on the genesis of carbonates from Martian meteorite ALH84001: Geochimica et Cosmochimica Acta, v. 62, p. 3–13.

Machel, H.G., and Burton, E.A., 1991, Factors governing cathodoluminescence in calcite and dolomite, and their implications for studies of carbonate diagenesis, *in* Barker, C.E., and Kopp, O.C., eds., Luminescence Microscopy and Spectroscopy: Quantitative and Qualitative Aspects: SEPM Short Course No. 25, p. 37–57.

Machel, H.G., Mason, R.A., Mariano, A.N., and Mucci, A., 1991, Causes and emission of luminescence in calcite and dolomite, *in* Barker, C.E., and Kopp, O.C., eds., Luminescence Microscopy and Spectroscopy: Qualitative and Quantitative Applications: SEPM Short Course No. 25, p. 9–25.

Mariano, A.N., 1988, Some further geological implications of cathodoluminescence, *in* Marshall, D.J., ed., Cathodoluminescence of Geological Materials: London, Unwin Hyman, p. 94–123.

Marshall, D.J., 1988, Cathodoluminescence of Geological Materials: London, Unwin Hyman, 146 p.

Onasch, C.M., and Venneman, T.W., 1995, Disequilibrium partitioning of oxygen isotopes associated with sector zoning in quartz: Geology, v. 23, p. 1103–1106.

Paquette, J., and Reeder, R.J., 1990, New type of compositional zoning in calcites: Insights into crystal-growth mechanisms: Geology, v. 18, p. 1244–1247.

Prezbindowski, D., 1980, Microsampling technique for stable isotopic analyses of carbonates: Journal of Sedimentary Petrology, v. 50, p. 643–644.

Rakovan, J., and Reeder, R.J., 1994, Differential incorporation of trace elements and dissymmetrization in apatite: the role of surface structure during growth: American Mineralogist, v. 79, p. 892–903.

Reeder, R.J., 1991, An overview of zoning in carbonate minerals, *in* Barker, C.E., and Kopp, O.C., eds., Luminescence Microscopy and Spectroscopy: Qualitative and Quantitative Applications: SEPM Short Course No. 25, p. 77–82.

Searle, A., 1990, Complex sector zonation in ankerite: Geochemical controls on crystal morphology and intersector element partitioning: Mineralogical Magazine, v. 54, p. 501–507.

Smalley, P.C., Stojfhorn, D.E., Raheim, A., Johansen, H., and Dickson, J.A.D., 1989, The laser microprobe and its application to the study of C and O isotopes in calcite and aragonite: Sedimentary Geology, v. 65, p. 257–273.

Spring, K.R., 2000, Scientific imaging with digital cameras: Biotechniques, v. 29, p. 70–76.

Wada, H., 1998, Microscale isotopic zoning in calcite and graphite crystals in marble: Nature, v. 1988, p. 61–63.

Wurster, C.M., Patterson, W.P., And Cheatham, M.M., 1999, Advances in micromilling techniques: a new apparatus for acquiring high-resolution oxygen and carbon stable isotope values and major/minor elemental ratios from accretionary carbonate: Computers and Geosciences, v. 25, p. 1159–1166.

Zinkernagel, U., 1979, Cathodoluminescence of quartz and its applications to sandstone petrography: Contributions to Sedimentology, v. 8, p. 1–6.

Received 13 December 1999; accepted 10 October 2000.